

Published in final edited form as:

Cell Rep. 2024 March 26; 43(3): 113938. doi:10.1016/j.celrep.2024.113938.

A therapeutically targetable positive feedback loop between *Inc-HLX-2-7*, HLX, and MYC that promotes group 3 medulloblastoma

Keisuke Katsushima^{1,2}, Kandarp Joshi^{1,2}, Menglang Yuan^{1,2}, Brigette Romero³, Mona Batish³, Stacie Stapleton², George Jallo², Elayaraja Kolanthai⁴, Sudipta Seal⁴, Olivier Saulnier^{5,6,7}, Michael D. Taylor^{8,9}, Robert J. Wechsler-Reya¹⁰, Charles G. Eberhart¹¹, Ranjan J. Perera^{1,2,12,*}

¹Department of Oncology, Sidney Kimmel Comprehensive Cancer Center, School of Medicine, Johns Hopkins University, 1650 Orleans St., Baltimore, MD 21231, USA

²Johns Hopkins All Children's Hospital, 600 5th St. South, St. Petersburg, FL 33701, USA

³Department of Medical and Molecular Sciences, University of Delaware, 15 Innovation Way, Newark, DE 19701, USA

⁴Advanced Materials Processing and Analysis Center, Nanoscience and Technology Center, Materials Science and Engineering, College of Medicine, University of Central Florida, Orlando, FL 32816, USA

⁵Genomics and Development of Childhood Cancers, Institut Curie, PSL University, 75005 Paris, France

⁶INSERM U830, Cancer Heterogeneity Instability and Plasticity, Institut Curie, PSL University, 75005 Paris, France

⁷SIREDO: Care, Innovation and Research for Children, Adolescents and Young Adults with Cancer, Institut Curie, 75005 Paris, France

8Texas Children's Cancer Center, Hematology-Oncology Section, Houston, TX 77004, USA

⁹Department of Pediatrics – Hematology/Oncology and Neurosurgery, Baylor College of Medicine, Houston, TX 77004, USA

¹⁰Herbert Irving Comprehensive Cancer Center, Columbia University Medical Center, New York, NY 10032, USA

AUTHOR CONTRIBUTIONS

Study design, K.K. and R.J.P.; experimental work, K.K., M.Y., B.R., M.B., and E.K.; provision of cell lines, patient samples, tissue microarrays, formalin-fixed, paraffin-embedded sections, and patient-derived xenografts for the study, C.G.E., and R.J.W.-R.; data analysis, K.J. and O.S.; nanoparticles and chemistry, E.K. and S. Seal; wrote the main draft of text, K.K., R.J.P., M.B., S. Stapleton, G.J., S. Seal, M.D.T., R.J.W.-R., and C.G.E.; revised and approved the final version of the manuscript, all authors.

SUPPLEMENTAL INFORMATION

Supplemental information can be found online at https://doi.org/10.1016/j.celrep.2024.113938.

DECLARATION OF INTERESTS

The authors declare no competing interests.

This is an open access article under the CC BY-NC license (http://creativecommons.org/licenses/by-nc/4.0/).

^{*}Correspondence: jperera2@jh.edu.

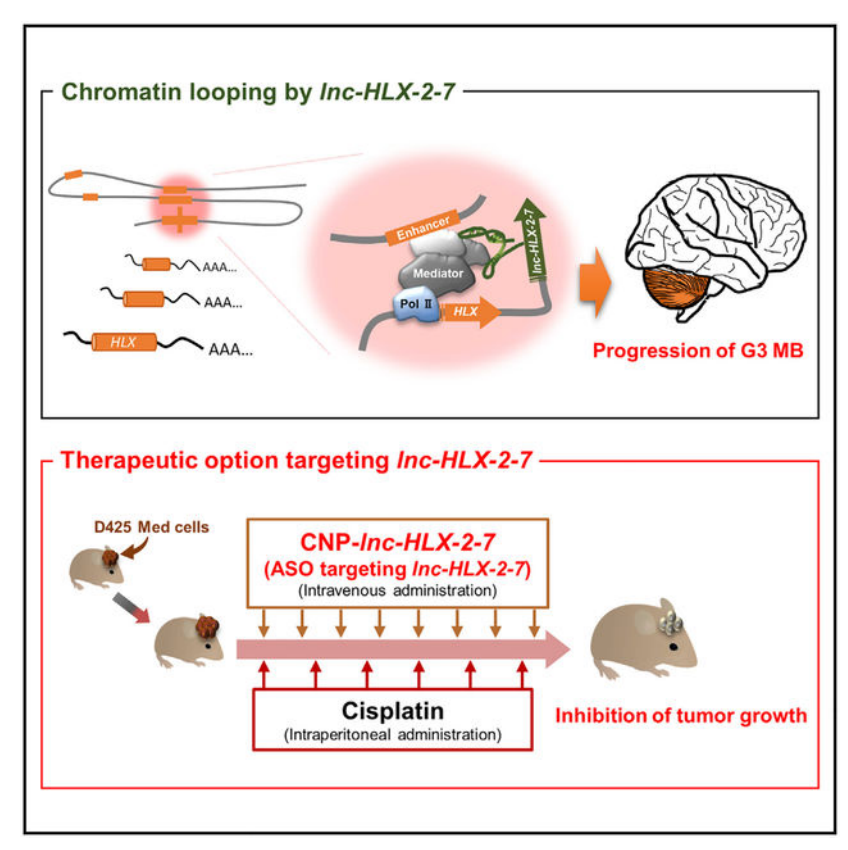
¹¹Department of Pathology, Johns Hopkins University School of Medicine, 720 Rutland Ave., Ross Bldg. 558, Baltimore, MD 21205, USA

¹²Lead contact

SUMMARY

Recent studies suggest that long non-coding RNAs (lncRNAs) contribute to medulloblastoma (MB) formation and progression. We have identified an lncRNA, *lnc-HLX-2-7*, as a potential therapeutic target in group 3 (G3) MBs. *lnc-HLX-2-7*RNA specifically accumulates in the promoter region of *HLX*, a sense-overlapping gene of *lnc-HLX-2-7*, which activates *HLX* expression by recruiting multiple factors, including enhancer elements. RNA sequencing and chromatin immunoprecipitation reveal that HLX binds to and activates the promoters of several oncogenes, including *TBX2*, *LIN9*, *HOXM1*, and *MYC*. Intravenous treatment with cerium-oxide-nanoparticle-coated antisense oligonucleotides targeting *lnc-HLX-2-7* (CNP-*lnc-HLX-2-7*) inhibits tumor growth by 40%–50% in an intracranial MB xenograft mouse model. Combining CNP-*lnc-HLX-2-7* with standard-of-care cisplatin further inhibits tumor growth and significantly prolongs mouse survival compared with CNP-*lnc-HLX-2-7* monotherapy. Thus, the *lnc-HLX-2-7-HLX-MYC* axis is important for regulating G3 MB progression, providing a strong rationale for using *lnc-HLX-2-7* as a therapeutic target for G3 MBs.

Graphical abstract



In brief

Katsushima et al. report that *Inc-HLX-2-7*RNA specifically accumulates in the HLX promoter region, where it activates HLX expression through recruitment of surrounding enhancers. This study provides a strong rationale for targeting *Inc-HLX-2-7* as a specific and potent therapeutic in group 3 medulloblastoma.

INTRODUCTION

Medulloblastoma (MB) is the most common malignant pediatric brain tumor. MB is categorized into four main molecular subgroups: wingless pathway (WNT) activated, sonic hedgehog pathway (SHH)-activated, group 3 (G3), and G4.^{2,3} Although the driver pathways for G3 and G4 MBs are not entirely clear, most of these tumors are characterized by c-Myc and MYCN signatures, respectively.^{3,4} Of the four subgroups, G3 MBs are the most aggressive, with a 45%–60% 5-year survival rate⁵ compared to >90% for WNT,⁶ 60%–80% for SHH,⁷ and 75%–80% for G4.⁵ respectively.

MBs are usually treated with surgical resection, radiotherapy, and chemotherapy. ⁸ Although craniospinal irradiation after surgery improves long-term outcomes, it is associated with significant long-term side effects and concerns about radio resistance and consequent progression or relapse. ⁹ Even with advanced molecular classification, the best subgroup-specific therapeutic targets in high-risk groups have yet to be determined. ¹⁰ There is an urgent need to identify specific molecular mechanisms in MB subgroups that can be exploited as targets for therapy.

MBs develop through a complex set of genetic, epigenetic, and non-coding RNA (ncRNA)-related mechanisms. ¹¹ However, the roles played by ncRNAs, particularly long ncRNAs (lncRNAs), in MB development remain poorly defined. A few lncRNAs have been implicated in MB. ¹² G3 MBs often harbor fusion of the *PVT1* oncogene, which encodes an lncRNA, with *MYC* and *NDRG1*, ¹³ and the lncRNA *TP73-AS1*, an antisense transcript of p73 mRNA, is upregulated in SHH MB, acting as an oncogene by sponging miR-493–3p. ^{14,15}

We previously reported upregulation of the lncRNA *lnc-HLX-2-7* (LNCipedia transcript ID: lnc-HLX-2:7, NONCODE v.4 ID: NONHSAT009630) in G3 MBs, with its knockdown (KD) reducing tumor growth both *in vitro* and *in vivo*. ¹⁶ Here, we elaborate on its mechanism of action and report that *lnc-HLX-2-7*RNA specifically accumulates in the *HLX* promoter region to activate HLX expression by recruiting a set of surrounding enhancer elements, thereby contributing to G3 MB tumor growth both *in vitro* and *in vivo*. Transcription and pathway analyses reveal that HLX directly binds to the promoters of many tumor-promoting genes, including *MYC*, and activates their expression. Furthermore, intravenous treatment with cerium oxide nanoparticle (CNP)-coupled antisense oligonucleotides (ASOs) targeting *lnc-HLX-2-7* (CNP-*lnc-HLX-2-7*) efficiently represses tumor growth in an intracranial MB xenograft mouse model. Finally, combination therapy with CNP-*lnc-HLX-2-7* and cisplatin further inhibits tumor growth and significantly prolongs mouse survival compared to CNP-*lnc-HLX-2-7* monotherapy. Our results highlight the importance of the *lnc-HLX-2-7-HLX-MYC* axis in regulating G3 MB, providing a

strong rationale for targeting *Inc-HLX-2-7* as a specific and potent therapeutic in patients with G3 MBs.

RESULTS

Inc-HLX-2-7 functions as an enhancer RNA (eRNA) to control HLX expression

Our previous work showed that *Inc-HLX-2-7* positively regulates the expression of the adjacent *HLX* gene and contributes to MB progression. ¹⁶ Because the *Inc-HLX-2-7* region is a G3-MB-specific enhancer region, ¹⁷ we hypothesized that *Inc-HLX-2-7* may function as an eRNA to control *HLX*. To gain mechanistic insights into how *Inc-HLX-2-7* regulates *HLX* expression, we conducted a global search for an *Inc-HLX-2-7*-binding protein. In an RNA-pull-down experiment, we incubated *in-vitro*-synthesized *Inc-HLX-2-7* labeled with bromouridine (BrU) with D425 Med cell extract and subjected the product to spectramass spectrometry (Figure S1A). A specific interaction of BrU-labeled *Inc-HLX-2-7* with the top-ranked interleukin enhancer-binding factor 3 (NF90, ILF3) was confirmed by ribonucleoprotein immunoprecipitation (Figure S1B). Cross-linking immunoprecipitation and qPCR analysis ¹⁸ revealed that NF90 directly binds to *Inc-HLX-2-7* (Figure S1C).

Next, we used the genome-wide chromatin isolation by RNA purification sequencing (ChIRP-seq) assay to map *Inc-HLX-2-7*-binding sites genome-wide in G3 MB cell lines. We designed biotinylated *Inc-HLX-2-7* oligonucleotides spanning the entire length of *Inc-HLX-2-7* exons and prepared chromatin from MED211 and D425 Med MB cells. We confirmed significant recovery of *Inc-HLX-2-7*RNA in *Inc-HLX-2-7*-pull-down samples and no recovery of LacZ (Figure 1A). Peak calling by model-based analysis for chromatin immunoprecipitation sequencing (ChIP-seq) revealed 528 putative *Inc-HLX-2-7*-binding sites genome-wide. Localization of *Inc-HLX-2-7*-binding sites revealed enrichment in intergenic and repetitive regions with an average length of 200–800 bp (Figure 1B; Table S1). DNA motif analysis of *Inc-HLX-2-7*-binding sites revealed four significantly enriched motifs with similar characteristics (Figure 1C). Interestingly, 14.7% of *Inc-HLX-2-7*-binding sites overlapped with potential NF90-occupied genes¹⁹ (Figure S1D). Surprisingly, approximately 40% of all probes bound upstream of the *HLX* gene adjacent to *Inc-HLX-2-7* in both MED211 and D425 Med cells (Figures 1D and 1E), strongly suggesting that *Inc-HLX-2-7*RNA exclusively accumulates in the *HLX* region.

Inc-HLX-2-7 activates HLX expression by recruiting surrounding enhancer elements

To elucidate how *Inc-HLX-2-7* regulates *HLX* expression, we first searched the *HLX* promoter and surrounding enhancer elements using the UCSC Genome Browser and GeneHancer²⁰ and found four potential enhancers (Figure 2A). Then, we conducted chromosome conformation capture analysis with restriction enzyme HindIII to evaluate the chromatin configuration involving *Inc-HLX-2-7* and these enhancer regions. Consequently, all possible combinations of re-ligated genomic fragments were formed between enhancer regions (*E1* and *E4*) and the HLX locus (Figure 2B). To validate interaction of *Inc-HLX-2-7* with the *HLX* promoter and the enhancers (*E1* and *E4*), we carried out simultaneous RNA-DNA fluorescence *in situ* hybridization using a set of primary and reporter probes for RNA and target DNA regions (Figure S2A). The DNA signal was intense but present in only

some cells, most likely because the highly compact nature of promoter and enhancer regions makes them inaccessible to the probes. Many of the sites that exhibited a DNA signal had a colocalizing signal for the lncRNA, providing single-molecule-resolution visual evidence of an interaction between *lnc-HLX-2-7* and the *HLX* promoter and enhancers (Figure S2B).

Next, we cloned the *E1* and *E4* enhancer regions into *HLX* promoter-luciferase reporter constructs to test whether these elements enhanced *HLX* promoter activity. We cloned the elements in forward or reverse directions downstream of the promoter-luciferase cassette to mimic potential enhancer activity (Figure 2C, left). Including these elements in constructs harboring the *HLX* promoter robustly induced luciferase reporter activity compared to the inclusion of the *HLX* promoter alone. To confirm that *Inc-HLX-2-7* is necessary for the increased promoter activity, we repeated the assay in MB cells in which *Inc-HLX-2-7* was knocked down (D425 Med *Inc-HLX-2-7*-KD and MED211 *Inc-HLX-2-7*-KD) and observed significantly reduced luciferase reporter activity (Figure 2C, right). Finally, to verify that *E1* and *E4* mediate the effect of *Inc-HLX-2-7* on *HLX*RNA, we targeted the *E1* and *E4* sequences in MB cell genomic DNA using CRISPR-Cas9 gene editing (Figure 2A). D425 Med and MED211 cells lacking the *E1* and *E4* sequences exhibited dramatic reductions in *HLX* mRNA levels (Figure 2D). Together, these data illustrate that *Inc-HLX-2-7* activates *HLX* expression by recruiting surrounding enhancer elements (Figure 2E).

HLX promotes oncogenic MB activities

Inc-HLX-2-7 specifically accumulated in the HLX promoter region and activated HLX expression (Figures 1 and 2). To evaluate the effect of HLX on tumor growth in vivo, we first established short hairpin RNA (shRNA) HLX-KD D425 Med and MED211 MB cells (sh-HLX #1 and #2) and control cell lines containing negative control shRNA (Figures 3A and 3B). Stable *HLX* KD significantly suppressed cell proliferation in D425 Med and MED211 cells (Figure 3C) but not in DAOY (SHH MB) or CHLA01 Med (G4 MB) cells (Figures S3D and S3E). Then, these cell lines were pre-infected with a lentivirus containing a luciferase reporter and were separately injected intracranially into the cerebellums of NOD-SCID mice (median survival time: 37 weeks).²¹ Weekly evaluation of tumor growth by bioluminescence imaging revealed significantly smaller tumors in mice transplanted with D425 Med and MED211 cells with HLXKD than in mice transplanted with control cells (n = 5, p < 0.05; Figures 3D and 3E). At day 28, Ki67 staining of tumor sections showed reduced cell proliferation in sh-HLX-expressing xenografts (p < 0.01; Figure 3F). Furthermore, HLX-KD tumors had a significantly higher percentage of TUNEL-positive cells than control xenografts (p < 0.01; Figure 3G). Kaplan-Meier plots showed that mice harboring HLX-KD xenografts had significantly prolonged survival than control mice (Figure 3H). Importantly, the same phenotype was observed in *Inc-HLX-2-7*-KD xenografts, as reported in our previous study. 16

Next, gene expression was measured by RNA sequencing in D425 Med cells expressing sh-HLX. Among 2,352 differentially expressed genes (false discovery rate < 0.05), 1,215 were upregulated and 1,137 were downregulated in cultured D425 Med *HLX*-KD cells (Figure S4A). Ingenuity Pathway Analysis (Qiagen) revealed that *HLX* KD preferentially affected genes associated with cell proliferation and G1/S phase transition, including *TBX2*,

LIN9, and FOXM1 signaling (Figures S4B and S4C), similar to our previous analysis of Inc-HLX-2-7-deficient cells. ¹⁶ Furthermore, HLX directly bound to the promoters of TBX2, LIN9, and FOXM1 and activated their expression (Figures S4D and S4E). To investigate the importance of HLX regulation by Inc-HLX-2-7 in G3 MB tumor growth, we performed rescue experiments of HLX in Inc-HLX-2-7-KD cells (Figure 4A). Consistently, reactivation of HLX recovered approximately 80% of the suppressed cell proliferation caused by Inc-HLX-2-7-KD in vitro and in vivo (Figures 4B–4D). For clinical correlation, we confirmed that (1) HLX is highly expressed in an independent cohort of human G3 MBs (Figure S5A), (2) HLX and Inc-HLX-2-7 expressions are highly correlated (Figure S5B), and (3) high HLX expression levels are associated with poor MB survival (Figure S5C). These results show that HLX downstream of Inc-HLX-2-7 regulates tumor growth in vivo and may function as an oncogene.

A positive feedback loop between Inc-HLX-2-7, HLX, and MYC strongly promotes G3 MB

Ingenuity Pathway Analysis of HLX-KD D425 Med cells suggested that HLX controls the expression of key transcription factors, including MYC. Our previous study showed that MYC positively regulates *Inc-HLX-2-7* expression and contributes to MB tumor progression. 16 Based on these findings, we hypothesized that *Inc-HLX-2-7*, HLX, and MYC are maintained in an interdependent manner. We therefore knocked down MYC and HLX by small interfering RNA in D425 Med and MED211 G3 MB cells, which decreased expression of both MYC and HLX when either was knocked down (Figures 5A-5C), suggesting interdependent regulation of HLX and MYC. Binding of HLX to the MYC promoter was further confirmed in an independent clinical cohort from the St. Jude Cloud²² (Figure S6A) and G3 MB line cells (Figure S6B). To further support this finding, we generated a G3 MB cell line lacking an MYC-binding motif (E-box; -CACGTG-) upstream of Inc-HLX-2-7, which can critically regulate the expression of Inc-HLX-2-7 in a doxycycline-dependent manner ¹⁶ (Figures 5D and 5E). As expected, the addition of doxycycline significantly decreased HLX and MYC expression in addition to Inc-HLX-2-7 (Figure 5E). Furthermore, E-box deficiency significantly reduced G3 MB proliferation in vitro and in vivo (Figures 5F-5H). Taken together, these results strongly suggest the presence of a functional positive feedback loop between Inc-HLX-2-7, HLX, and MYC (Figure S6C) in G3 MB.

CNP-Inc-HLX-2-7 represses tumor growth in an intracranial MB xenograft mouse model

Next, we investigated the therapeutic effect of an ASO targeting *lnc-HLX-2-7* in an intracranial xenograft mouse model. D425 Med cells were injected into the brains of NOD-SCID mice. After 14 days, CNP-*lnc-HLX-2-7* was administered intravenously every 3 days for 24 days (Figure 6A). CNP-*lnc-HLX-2-7* accumulated in brain tumors and was retained for at least 24 h (Figure S7). Treatment with CNP-*lnc-HLX-2-7* markedly reduced tumor growth compared to control ASO coated with CNP (CNP-CTRL) and downregulated *lnc-HLX-2-7* expression (p < 0.01; Figures 6B–6D). Consistently, in CNP-*lnc-HLX-2-7*-treated xenografts, protein expression of MYC and HLX was significantly decreased (Figure 6E). CNP-*lnc-HLX-2-7*-treated mice had significantly longer survival than control mice (Figure 6F). Taken together, these data provide a strong rationale for using *lnc-HLX-2-7* as a specific and potent therapeutic target for G3 MBs.

Combination therapy of CNP-Inc-HLX-2-7 and cisplatin inhibits tumor growth and prolongs mouse survival

Next, we analyzed whether there was a synergistic action between CNP-*Inc-HLX-2-7* and cisplatin, often used as an adjuvant chemotherapeutic in children with MB. The IC₅₀ for cisplatin in *Inc-HLX-2-7*-KD D425 Med cells was lower than that in controls (Figure S8), suggesting that combining cisplatin with CNP-*Inc-HLX-2-7* might be more effective than administering CNP-*Inc-HLX-2-7* alone. To test this hypothesis, we examined the effect of combination cisplatin and CNP-*Inc-HLX-2-7* therapy in the intracranial xenograft mouse model *in vivo*. D425 Med cells were injected into the brains of NOD-SCID mice, and after 14 days, mice were treated intravenously with CNP-*Inc-HLX-2-7* (every 3 days for 24 days) and/or cisplatin (every 4 days for 24 days) (Figure 7A). CNP-*Inc-HLX-2-7* significantly suppressed tumor growth compared to CNP-CTRL and cisplatin (Figures 7B and 7C). Combination therapy with cisplatin and CNP-*Inc-HLX-2-7* further suppressed tumor growth, induced apoptosis, suppressed the expression of MYC target genes, and improved mouse survival compared to CNP-*Inc-HLX-2-7* alone (Figure S9).

DISCUSSION

Here, we show that *Inc-HLX-2-7*RNA specifically accumulates in the *HLX* promoter region, where it activates HLX expression through recruitment of surrounding enhancers. HLX subsequently directly binds to the promoters and activates many tumor-promoting genes, including *MYC*. Suppressing this mechanism through intravenous treatment with CNP-*Inc-HLX-2-7* represses tumor growth in an intracranial MB xenograft mouse model, while combined therapy with CNP-*Inc-HLX-2-7* and cisplatin enhances the tumor-growth-inhibiting effect of CNP-*Inc-HLX-2-7* and significantly prolongs mouse survival.

Despite the crucial role of MYC in G3 MB, development of an MYC-directed therapy has proven elusive because of its complex structure and nonenzymatic/pleiotropic properties.²³ However, targeting epigenetic regulators of MYC may offer a promising alternative. Bromodomain and extra-terminal (BET)-containing proteins promote transcription by recognizing side-chain-acetylated lysines on open chromatin and have been shown to be potential MYC transcription targets.²⁴ Nevertheless, BET inhibitor resistance is common through several resistance mechanisms in different cancer types, ^{25,26} including through an HLX-mediated mechanism in G3 MB.²⁷ In this study, we discovered that Inc-HLX-2-7 controls *HLX* expression and contributes to G3 MB growth and suppression of apoptosis. Thus, *Inc-HLX-2-7* may also influence BET inhibitor resistance. We postulate that in addition to acting as a therapeutic in its own right, CNP-Inc-HLX-2-7 may also provide a solution to BET inhibitor resistance, a hypothesis that requires further investigation. Notably, our analysis showed that HLX directly binds to the promoters of TBX2, LIN9, and FOXM1, which are associated with cell proliferation and G1/S phase transition, ^{28–32} activating their expression (Figures S3D and S3E) in addition to MYC. These cell-cycle-regulating activities are likely to be a major reason why *Inc-HLX-2-7* and HLX inhibition strongly reduce G3 MB proliferation in vitro and in vivo.

Our results propose a model for *Inc-HLX-2-7*-mediated chromatin loops that function as eRNAs in the transcriptional activation of *HLX*. Interestingly, many eRNAs have been

shown to be overexpressed in tumor samples compared to adjacent normal tissue.^{33,34} This phenomenon raises the possibility of therapeutically targeting eRNAs to overcome enhancer overactivation in cancer. ASOs targeting specific eRNAs have been shown to effectively inhibit gene targeting and tumor growth in many cancer types.^{34–36} Importantly, the high specificity of eRNAs makes them advantageous as drug targets because their inhibition, at least in theory, will not affect other inappropriate tissues.

The successful application of RNA-based therapeutics requires an interdisciplinary approach including technical advancements in molecular biology, immunology, pharmacology, chemistry, and nanotechnology. Several steps remain before clinical application of CNP-*Inc-HLX-2-7* is realized; for example, extensive testing for immunogenicity against CNP-*Inc-HLX-2-7*, developing chemical ASO modifications to improve pharmacokinetics and pharmacodynamics, and determination of CNP-*Inc-HLX-2-7* biodistribution. Investigation and consideration of any intracellular escape mechanisms of CNP-*Inc-HLX-2-7* and examination of their optimal dosage are also necessary.

Nevertheless, our results highlight the importance of the *Inc-HLX-2-7-HLX-MYC* axis in G3 MB and provide a strong rationale for targeting *Inc-HLX-2-7* as a specific and potent therapeutic approach in children with G3 MB.

Limitations of the study

Although we focused on regulation of *HLX* by *Inc-HLX-2-7*, ChIRP-seq analysis revealed approximately 550 putative *Inc-HLX-2-7*-binding sites genome-wide (Figure 1B). *Inc-HLX-2-7* might therefore act not only in *cis* but also in *trans* to regulate gene expression. The functions and regulatory mechanisms of *Inc-HLX-2-7* in *trans* require further investigation. Figure 3E depicts the tendency for tumor growth to increase 21 days after transplantation with *HLX*-KD D425 Med cells. This could be due to the inherent property changes of D425 Med cells under long-term *in vivo* environment, but further investigation is warranted. Also, intravenous treatment with CNP-*Inc-HLX-2-7* efficiently repressed tumor growth in an intracranial MB xenograft mouse model, so our conclusions on efficacy are limited to a xenograft model using immunodeficient mice (NOD-SCID mice). Future pre-clinical investigations should analyze the anti-tumor effect of CNP-*Inc-HLX-2-7* in immunocompetent mouse models, such as the spontaneous G3 MB mouse model, with a view to future clinical translation.

STAR*METHODS

RESOURCE AVAILABILITY

Lead contact—Further information and requests for resources and reagents should be directed to and will be fulfilled by the lead contact, Ranjan J. Perera (jperera2@jh.edu).

Materials availability—Materials generated in this study will be made available on request.

Data and code availability

RNA-seq data described in the manuscript are accessible at NCBI GEO accession number GSE188746. ChIRP-seq data for genomic maps of *Inc-HLX-2-7* manuscript are accessible at NCBI GEO accession number GSE232749.

- This paper does not report original code.
- Any additional information required to reanalyze the data reported in this work paper is available from the lead contact upon request

EXPERIMENTAL MODEL AND STUDY PARTICIPANT DETAILS

Cell culture—Cell lines were authenticated by using single tandem repeat profiling. D425 Med cells were cultured in DMEM/F12 with 10% FBS and 1% penicillin/streptomycin. MED211 cells were cultured in DMEM/F12 medium supplemented with B27 supplement (Thermo Fisher Scientific, Waltham, MA), 5 mg/mL heparin, 20 ng/mL EGF (R&D Systems, Minneapolis, MN), and 20 ng/mL bFGF (R&D Systems, Minneapolis, MN). DAOY cells were cultured in DMEM with 10% serum and 1% penicillin/streptomycin. CHLA01 Med cells were cultured in DMEM/F12 medium supplemented with B27 supplement, 20 ng/mL EGF, and 20 ng/mL bFGF. All cells were grown in a humidified incubator at 37°C with 5% CO₂.

MB xenografts (intracranial)—All mouse studies were approved by and performed in accordance with the policies and regulations of the Animal Care and Use Committee of Johns Hopkins University. Intracranial MB xenografts were established by injecting D425 Med and MED211 cells into the cerebellums of 6–8 weeks old female NOD-SCID mice (Jackson Laboratory, Bar Harbor, ME). Cerebellar coordinates were –2 mm from lambda, +1 mm laterally, and 1.5 mm deep. Tumor growth was evaluated by weekly bioluminescence imaging with an *in vivo* spectral imaging system (IVIS Lumina II, Xenogen, Alameda, CA).

METHOD DETAILS

ChIRP oligonucleotide design—Biotinylated 20-mer antisense oligonucleotides were designed with Stellaris smFISH probe designer (http://biosearch.com/). Designed probes were compared with the human genome using the BLAST tool, and probes returning only target were selected.

ChIRP—Cells were cross-linked with 0.3% formaldehyde for 10 min, quenched with 0.125 M glycine for 5 min, and washed with phosphate-buffered saline. Sheared chromatin was prepared by sonication in a Bioruptor 300 (Diagenode, Liege, Belgium) to produce DNA between 100 and 500 bp. Chromatin was diluted three times with hybridization buffer, and probes were added (15 pmol per chromatin from 1 million cells). The mixture was incubated overnight at 37°C with rotation. Streptavidin magnetic C1 beads (Thermo Fisher Scientific) were added and mixed for another 2 h at 37°C. After extensive washing, the beads were resuspended in a buffer containing proteinase K (Sigma-Aldrich, St Louis, MO) and incubated at 50°C for 45 min, followed by overnight incubation at 65°C for reverse cross-linking. Beads were resuspended in 3× original volume DNA elution buffer

(50 mM NaHCO₃, 1% SDS, 200 mM NaCl), and DNA was eluted with a cocktail of 100 μ g/mL RNase A (Thermo Fisher Scientific) and 0.1 U/ μ L RNase H (Thermo Fisher Scientific). DNA was then purified using the ChIP DNA Clean and concentrator kit (Zymo Research, Irvine, CA). Purified DNA was processed for high-throughput sequencing library preparation.

Chromosome conformation capture—Cells were cross-linked with 2% formaldehyde and lysed with cell lysis buffer. An aliquot of nuclei (1×10⁷) was digested with 1000 U HindIII (NEB) at 37°C overnight. Chromatin DNA was diluted with NEB ligation buffer and ligated with 4000 U of T4 DNA ligase. After reversing the cross-links, DNA was purified and used for PCR amplification with primers derived from different regions of the *HLX* locus. The 3C PCR products were cloned and sequenced to validate the intrachromosomal interaction by checking for the presence of the HindIII ligation site. The 3C interaction was quantified by qPCR and was standardized over the 3C ligation control locus. Primer sequences are listed in the Table S2.

ASO-Inc-HLX2-7—ASOs were designed with the Integrated DNA Technologies (IDT) Antisense Design Tool (IDT, Coralville, IA). ASO knockdowns were prepared with 50 nM (final concentration) locked nucleic acid (LNA) GapmeRs transfected with Lipofectamine 3000 (Thermo Fisher Scientific). All ASOs were modified with phosphorothioate (PS) linkages. The following ASOs were used: ASO targeting *Inc-HLX-2-7* (ASO-*Inc-HLX-2-7*): +T*+G*+A*G*A*T*T*A*A*T*C*T*A*G*A*T*+T*+G*+C and control ASO (ASO-*CTRL*): +T*+C*+G*A*A*G* T*A*C*T*C*A*G*C*G*T*A*A*+G*+T*+T. The PS linkages are indicated with asterisks (*), and LNA-modified oligonucleotides are indicated with plus signs (+).

Quantitative real-time PCR—To obtain RNA from xenografts, we first pulverized the tumor tissues and then purified the total RNA with the Direct-zol RNA Miniprep kit (Zymo Research, Irvine, CA). Quantitative PCR was carried out with SYBR Green mRNA assays as previously described.³⁸ Primer sequences are listed in the Table S2.

Luciferase reporter gene assays—The promoter and enhancer elements of *HLX* were cloned into pGL4.10 vector (Promega, Madison, WI) using an In-Fusion HD cloning kit (Takara Bio, Mountain View, CA). The recombinant pGL4.10 plasmids were transfected into cells using Lipofectamine 3000 (Thermo Fisher Scientific). At 48 h post-transfection, both firefly and Renilla luciferase activities were measured using the Dual-Glo Luciferase Assay (Promega) in a GloMax 20/20 luminometer (Promega). Firefly luciferase activity was normalized to Renilla luciferase activity.

Lentivirus packaging and stable cell line establishment—The HLX-knockdown or HLX-expressing lentivirus plasmids (GeneCopoeia, Rockville, MD) were packaged into 293T cells using Lenti-X Packaging Single Shots (Takara Bio) according to the manufacturer's instructions. For lentivirus infection, cells were incubated with viral supernatant for 24 h, followed by 5 μ g/mL blasticidin (InvivoGen, San Diego, CA) or 1 μ g/mL puromycin (InvivoGen) selection until drug-resistant colonies became visible.

siRNA-mediated knockdown—siRNAs targeting *HLX* (catalog no. 4427037, ID: s6639) and *MYC* (catalog no. 4427037, ID: s9129) were purchased from Thermo Fisher Scientific. siRNAs were transfected at 20 nM for 48 h using Lipofectamine RNAiMAX (Thermo Fisher Scientific). The efficiency was determined by qRT-PCR.

Western blotting—Cell lysates were fractionated by SDS-polyacrylamide gel electrophoresis and transferred to polyvinylidene difluoride membranes. Membranes were blocked with 5% bovine serum albumin (Fisher Scientific, Hampton, NH) in TBST buffer (10 mM Tris, pH 8.0; 150 mM NaCl; 0.5% Tween 20) for 60 min and then incubated with antibodies targeting HLX (cat. HPA005968, 1:200, Sigma-Aldrich), MYC (cat. 5605, 1:500, Cell Signaling Technology, Danvers, MA), cleaved Caspase-7 (Asp198) (cat. 8438, 1:1000, Cell Signaling Technology), cleaved Caspase-3 (Asp175) (cat. 9661, 1:1000, Cell Signaling Technology), and GAPDH (cat. GTX100118, 1:5000, Genetex, Irvine, CA) at 4°C overnight. Membranes were washed and incubated with a 1:10,000 dilution of horseradish peroxidase—conjugated anti-mouse or anti-rabbit antibodies for 1 h. Blots were washed and developed with the ECL system (Thermo Fisher Scientific) according to the manufacturer's protocols.

Immunohistochemistry—For the analysis of cell proliferation, tumor sections were incubated with anti-Ki67 (Alexa Fluor 488 conjugate) antibodies (cat. 11882, 1:200, Cell Signaling Technology, Danvers, MA) at 4°C overnight. Apoptosis in the tumor sections was analyzed with the DeadEnd Fluorometric TUNEL System (Promega) according to the manufacturer's instructions. The stained sections were imaged with a confocal laser-scanning microscope (Nikon C1 confocal system, Nikon Corp, Tokyo, Japan). The acquired images were processed with NIS (Nikon) and analyzed with ImageJ software (https://imagej.nih.gov/ij/).

Chromatin immunoprecipitation (ChIP)—Cells (1×10^6) were treated with 1% formaldehyde for 8 min to crosslink histones to DNA. Cell pellets were resuspended in lysis buffer (1% SDS, 10 mmol/L EDTA, 50 mmol/L Tris-HCl pH 8.1, and protease inhibitor) and sonicated using a Covaris S220 system (Covaris Inc., Woburn, MA). After diluting the cell lysate 1:10 with dilution buffer (1% Triton X-, 2 mmol/L EDTA, 150 mmol/L NaCl, 20 mmol/L Tris-HCl pH 8.1), diluted cell lysates were incubated for 16 h at 4°C with Dynabeads Protein G (Thermo Fisher Scientific) precoated with 5 μ L of anti-HLX antibody (cat. HPA005968, 1:200, Sigma-Aldrich). ChIP products were analyzed by SYBR Green ChIP-qPCR using the primers listed in Table S2.

Identification of *Inc-HLX-2-7*—binding proteins—*Inc-HLX-2-7*—binding proteins were purified with the RiboTrap kit (MBL International, Woburn, MA) according to the manufacturer's protocol. Briefly, 1×10^7 cells were harvested and lysed in CE buffer with detergent solution. After the cytosolic fraction was removed, nuclei were resuspended in NE buffer. The nuclear lysate was used for immunoprecipitation. BrU-labeled *Inc-HLX-2-7* was prepared with the MEGAstrip T7 system (Thermo Fisher Scientific). BrU-labeled RNA was mixed with the nuclear extracts and captured by Protein G agarose conjugated with an anti-BrdU antibody. Proteins were digested with trypsin for analysis by mass spectrometry

performed by the Johns Hopkins University School of Medicine Proteomics Core (https://www.hopkinsmedicine.org/research/labs/mass-spectrometry-core). Average peptide numbers between replicates were used for determining the specific binding partners. To measure the degree of variation between replicates, we calculated the coefficient of variation as the ratio of the standard deviation to the mean [(Standard deviation/mean)×100].

RIP analysis—RIP analysis was carried out with the RiboCluster Profiler RIP-Assay kit (MBL International, Woburn, MA) according to the manufacturer's protocol. RNA-protein complexes were immunoprecipitated with an anti-NF90 antibody (cat. 19887–1-AP, Protein-tech); anti-IgG antibody was used as a negative control (MBL International). Immunoprecipitated RNA was then analyzed by qPCR with the primers listed in Table S2. Results were normalized by the percentage of non-immunoprecipitated input RNA in each sample.

Cross-linking immunoprecipitation and qPCR (CLIP-qPCR) analysis—The CLIP assay was performed as previously ¹⁸ with the following modifications. Briefly, cells were cross-linked once at 150 mJ/cm² using 254 nm UV light with a CX-2000 Ultraviolet Crosslinker (UVP) before being lysed. After lysis, cells lysates were treated with RNase T1 (final concentration 500 U/mL, Thermo Fisher Scientific) for 6 min and then subjected to immunoprecipitation with an anti-NF90 or IgG antibody following a standard RIP protocol. ¹⁸ After reverse transcription, the resulting cDNA was subjected to qPCR. The primers used for qPCR are listed in Table S2. The amount of immunoprecipitated RNAs in each sample is represented as signal relative to that from the negative (IgG) sample.

Simultaneous single-molecule RNA and DNA FISH—Non-adherent D425 Med cells were fixed, permeabilized, and washed to prepare for hybridization³⁹ with the following modification. Reporter probes were used to target the "tails" added to unlabeled primary probes designed to bind the HLX promoter, enhancer 1 (E1), or enhancer 4 (E4) for DNA FISH, whereas, for RNA FISH, a primary probe set was designed to bind to the entire length of Inc-HLX-2-7. The reporter probes for DNA were labeled with Texas Red, and probes for RNA were labeled with Cy5. The probe sequences are provided in Table S3. Imaging involved four sequential steps: (1) cells were hybridized with RNA primary probes overnight, washed, and then hybridized with RNA reporter probes; (2) the cell pellet was washed, and immunofluorescence was performed with anti-Cy5 antibody (cat. sc-166896, Santa Cruz Biotechnology, Dallas, TX). 40 Then, the cells were fixed with formaldehyde to cross-link the antibody signal reporting the location of RNA⁴¹; (3) the cell pellet was treated with formamide and high temperature, and DNA FISH was performed, ⁴² and (4) the cells were suspended in DAPI-containing mounting medium, placed on a glass slide, covered with a coverslip, and sealed with clear nail polish. The cells were imaged with a 100× oil objective on a Nikon TiE inverted fluorescence microscope equipped with Pixis 1024b (Princeton Instruments, Inc., Trenton, NJ) and Metamorph imaging software (Molecular Devices, San Jose, CA). The images were analyzed by ImageJ software.

CNP-*Inc-HLX-2-7* **synthesis and characterization—**The cerium oxide nanoparticles (CNPs) were synthesized using wet-chemical hydrolysis method at room temperature. ⁴³

Five mM of cerium nitrate hexahydrate with a purity of 99.999% was dissolved in 48 mL of deionized water followed by the addition of 2 mL of hydrogen peroxide to the cerium solution. The solution was continuously mixed for 5 min. After the addition of hydrogen peroxide, the solution turned yellow and gradually became white after eight weeks of aging at room temperature. The fully aged nanoparticles were used for conjugation. For ASO-*Inc-HLX-2-7* conjugation with CNPs, initially, 270 μ L of DMSO was taken in a 2 mL centrifuge tube, 44 to which 30 μ L of CNPs (5 mM) were then added. The OH group on the CNP surface was activated using 30 μ L of CDI (500 mM) solution. After shaking the mixture for 1 h, 150 μ L of ASO-*Inc-HLX-2-7* (200 μ M) was added to the activated CNP solution. The solution was mixed thoroughly by pipetting, and then 3790 μ L of sodium borate buffer (10 mM, pH 8.5) was added. The solution was shaken at room temperature for 3 h. Following shaking, the solution was transferred into a 50 mL dialysis tube and dialyzed against RNase-free water at 4°C for 20 h to remove the free miR-211 and DMSO solvent. The RNase-free water was replaced 2 h after starting dialysis. After dialysis, samples were collected and stored at -20° C until further use.

Therapeutic experiment with CNP-*Inc-HLX-2-7*—D425 Med cells were injected intracranially into 6-week-old NOD-SCID mice. Two weeks after the injection, CNP-*CTRL* (n = 10) or CNP-*Inc-HLX-2-7* (n = 10; 1 mg/kg per day) was injected intravenously twice a week for 3 weeks. The accumulation of ASOs in tumor tissue was confirmed by an *in vivo* spectral imaging system (IVIS Lumina II, Xenogen Corp, Cranbury, NJ). Tumor growth was evaluated every 3 days by bioluminescence imaging with the IVIS Lumina II.

QUANTIFICATION AND STATISTICAL ANALYSIS

Statistical analyses were carried out with GraphPad Prism software (GraphPad Software, Ja Jolla, CA) and Limma R package. Data are presented as mean ± SD of three independent experiments. Differences between two groups were analyzed by the paired Student's t test. Kruskal–Wallis analysis was used to evaluate differences between more than two groups.

Supplementary Material

Refer to Web version on PubMed Central for supplementary material.

ACKNOWLEDGMENTS

We acknowledge the Johns Hopkins University proteomics core for conducting mass spectrometry analysis to identify *Inc-HLX-2-7* binding partners, Dr. Rudramani Pokhrel for support of data analysis, and Ms. Tiffany Casey for administrative support and manuscript submission. This work was supported by the Schamroth Project funded by Ian's Friends Foundation to R.J.P. and G.J.; a grant from the Hough Foundation to R.J.P. and G.J.; grant P30 CA006973 (Johns Hopkins University Sidney Kimmel Comprehensive Cancer Center) to R.J.P. and C.G.E.; grant NCI 5P30CA030199 (Sanford-Burnham Prebys Medical Discovery Institute) to R.J.W.-R.; grant R01NS124668-01A1 to R.J.P.; grant R35 NS122339 to R.J.W.-R.; and a CPRIT Scholar award from the MD Anderson Cancer Center to M.D.T.

REFERENCES

1. Louis DN, Perry A, Reifenberger G, von Deimling A, Figarella-Branger D, Cavenee WK, Ohgaki H, Wiestler OD, Kleihues P, and Ellison DW (2016). The 2016 World Health Organization

- Classification of Tumors of the Central Nervous System: a summary. Acta Neuropathol 131, 803–820. 10.1007/s00401-016-1545-1. [PubMed: 27157931]
- 2. Cavalli FMG, Remke M, Rampasek L, Peacock J, Shih DJH, Luu B, Garzia L, Torchia J, Nor C, Morrissy AS, et al. (2017). Intertumoral Heterogeneity within Medulloblastoma Subgroups. Cancer Cell 31, 737–754.e6. 10.1016/j.ccell.2017.05.005. [PubMed: 28609654]
- 3. Northcott PA, Shih DJH, Remke M, Cho YJ, Kool M, Hawkins C, Eberhart CG, Dubuc A, Guettouche T, Cardentey Y, et al. (2012). Rapid, reliable, and reproducible molecular sub-grouping of clinical medulloblastoma samples. Acta Neuropathol 123, 615–626. 10.1007/s00401-011-0899-7. [PubMed: 22057785]
- Northcott PA, Buchhalter I, Morrissy AS, Hovestadt V, Weischenfeldt J, Ehrenberger T, Gröbner S, Segura-Wang M, Zichner T, Rudneva VA, et al. (2017). The whole-genome landscape of medulloblastoma subtypes. Nature 547, 311–317. 10.1038/nature22973. [PubMed: 28726821]
- Shih DJH, Northcott PA, Remke M, Korshunov A, Ramaswamy V, Kool M, Luu B, Yao Y, Wang X, Dubuc AM, et al. (2014). Cytogenetic prognostication within medulloblastoma subgroups. J. Clin. Oncol 32, 886–896. 10.1200/JCO.2013.50.9539. [PubMed: 24493713]
- Ramaswamy V, Remke M, Adamski J, Bartels U, Tabori U, Wang X, Huang A, Hawkins C, Mabbott D, Laperriere N, et al. (2016). Medulloblastoma subgroup-specific outcomes in irradiated children: who are the true high-risk patients? Neuro Oncol 18, 291–297. 10.1093/neuonc/nou357. [PubMed: 25605817]
- Northcott PA, Korshunov A, Pfister SM, and Taylor MD (2012). The clinical implications of medulloblastoma subgroups. Nat. Rev. Neurol 8, 340–351. 10.1038/nrneurol.2012.78. [PubMed: 22565209]
- 8. Grassiot B, Beuriat PA, Di Rocco F, Leblond P, Faure-Conter C, Szathmari A, and Mottolese C (2021). Surgical management of posterior fossa medulloblastoma in children: The Lyon experience. Neurochirurgie 67, 52–60. 10.1016/j.neuchi.2021.01.003. [PubMed: 33482236]
- 9. Grill J, Dufour C, Guerrini-Rousseau L, and Ayrault O (2021). New research directions in medulloblastoma. Neurochirurgie 67, 87–89. 10.1016/j.neuchi.2019.01.002. [PubMed: 30904166]
- Perreault S, Ramaswamy V, Achrol AS, Chao K, Liu TT, Shih D, Remke M, Schubert S, Bouffet E, Fisher PG, et al. (2014). MRI surrogates for molecular subgroups of medulloblastoma. AJNR. Am. J. Neuroradiol 35, 1263–1269. 10.3174/ajnr.A3990. [PubMed: 24831600]
- Suzuki H, Kumar SA, Shuai S, Diaz-Navarro A, Gutierrez-Fernandez A, De Antonellis P, Cavalli FMG, Juraschka K, Farooq H, Shibahara I, et al. (2019). Recurrent noncoding U1 snRNA mutations drive cryptic splicing in SHH medulloblastoma. Nature 574, 707–711. 10.1038/ s41586-019-1650-0. [PubMed: 31664194]
- 12. Katsushima K, Jallo G, Eberhart CG, and Perera RJ (2021). Long non-coding RNAs in brain tumors. NAR Cancer 3, zcaa041. 10.1093/narcan/zcaa041. [PubMed: 34316694]
- 13. Northcott PA, Shih DJH, Peacock J, Garzia L, Morrissy AS, Zichner T, Stütz AM, Korshunov A, Reimand J, Schumacher SE, et al. (2012). Subgroup-specific structural variation across 1,000 medulloblastoma genomes. Nature 488, 49–56. 10.1038/nature11327. [PubMed: 22832581]
- Varon M, Levy T, Mazor G, Ben David H, Marciano R, Krelin Y, Prasad M, Elkabets M, Pauck D, Ahmadov U, et al. (2019). The long non-coding RNA TP73-AS1 promotes tumorigenicity of medulloblastoma cells. Int. J. Cancer 145, 3402–3413. 10.1002/ijc.32400. [PubMed: 31081944]
- Li B, Shen M, Yao H, Chen X, and Xiao Z (2019). Long Noncoding RNA TP73-AS1 Modulates Medulloblastoma Progression In Vitro And In Vivo By Sponging miR-494-3p And Targeting EIF5A2. OncoTargets Ther 12, 9873-9885. 10.2147/OTT.S228305.
- Katsushima K, Lee B, Kunhiraman H, Zhong C, Murad R, Yin J, Liu B, Garancher A, Gonzalez-Gomez I, Monforte HL, et al. (2021). The long noncoding RNA *Inc-HLX-2-7* is oncogenic in Group 3 medulloblastomas. Neuro Oncol 23, 572–585. 10.1093/neuonc/noaa235. [PubMed: 33844835]
- Lin CY, Erkek S, Tong Y, Yin L, Federation AJ, Zapatka M, Haldipur P, Kawauchi D, Risch T, Warnatz H-J, et al. (2016). Active medulloblastoma enhancers reveal subgroup-specific cellular origins. Nature 530, 57–62. 10.1038/nature16546. [PubMed: 26814967]

18. Yoon J-H, and Gorospe M (2016). Cross-linking immunoprecipitation and qPCR (CLIP-qPCR) analysis to map interactions between long non-coding RNAs and RNA-binding proteins. Methods Mol. Biol 1402, 11–17. [PubMed: 26721479]

- Wu TH, Shi L, Adrian J, Shi M, Nair RV, Snyder MP, and Kao PN (2018). NF90/ILF3 is a transcription factor that promotes proliferation over differentiation by hierarchical regulation in K562 erythroleukemia cells. PLoS One 13, e0193126. 10.1371/journal.pone.0193126. [PubMed: 29590119]
- 20. Fishilevich S, Nudel R, Rappaport N, Hadar R, Plaschkes I, Iny Stein T, Rosen N, Kohn A, Twik M, Safran M, et al. (2017). GeneHancer: Genome-wide Integration of Enhancers and Target Genes in GeneCards. Database (Oxford) 2017, bax028. 10.1093/database/bax028. [PubMed: 28605766]
- Shultz LD, Schweitzer PA, Christianson SW, Gott B, Schweitzer IB, Tennent B, McKenna S, Mobraaten L, Rajan TV, and Greiner DL (1995). Multiple defects in innate and adaptive immunologic function in NOD/LtSz-scid mice. J. Immunol. (Baltimore, Md.: 1950) 154, 180–191.
- 22. McLeod C, Gout AM, Zhou X, Thrasher A, Rahbarinia D, Brady SW, Macias M, Birch K, Finkelstein D, Sunny J, et al. (2021). St. Jude Cloud: A Pediatric Cancer Genomic Data-Sharing Ecosystem. Cancer Discov 11, 1082–1099. 10.1158/2159-8290.Cd-20-1230. [PubMed: 33408242]
- 23. Llombart V, and Mansour MR (2022). Therapeutic targeting of "undrug-gable" MYC. EBioMedicine 75, 103756. 10.1016/j.ebiom.2021.103756. [PubMed: 34942444]
- 24. Delmore JE, Issa GC, Lemieux ME, Rahl PB, Shi J, Jacobs HM, Kastritis E, Gilpatrick T, Paranal RM, Qi J, et al. (2011). BET bromodomain inhibition as a therapeutic strategy to target c-Myc. Cell 146, 904–917. 10.1016/j.cell.2011.08.017. [PubMed: 21889194]
- Fong CY, Gilan O, Lam EYN, Rubin AF, Ftouni S, Tyler D, Stanley K, Sinha D, Yeh P, Morison J, et al. (2015). BET inhibitor resistance emerges from leukaemia stem cells. Nature 525, 538–542. 10.1038/nature14888. [PubMed: 26367796]
- Shu S, Lin CY, He HH, Witwicki RM, Tabassum DP, Roberts JM, Janiszewska M, Huh SJ, Liang Y, Ryan J, et al. (2016). Response and resistance to BET bromodomain inhibitors in triple-negative breast cancer. Nature 529, 413–417. 10.1038/nature16508. [PubMed: 26735014]
- 27. Bandopadhayay P, Piccioni F, O'Rourke R, Ho P, Gonzalez EM, Buchan G, Qian K, Gionet G, Girard E, Coxon M, et al. (2019). Neuronal differentiation and cell-cycle programs mediate response to BET-bromodomain inhibition in MYC-driven medulloblastoma. Nat. Commun 10, 2400. [PubMed: 31160565]
- 28. Lu S, Louphrasitthiphol P, Goradia N, Lambert JP, Schmidt J, Chauhan J, Rughani MG, Larue L, Wilmanns M, and Goding CR (2021). TBX2 controls a proproliferative gene expression program in melanoma. Genes Dev 35, 1657–1677. 10.1101/gad.348746.121. [PubMed: 34819350]
- Iness AN, and Litovchick L (2018). MuvB: A Key to Cell Cycle Control in Ovarian Cancer. Front. Oncol 8, 223. 10.3389/fonc.2018.00223. [PubMed: 29942794]
- 30. Prince S, Carreira S, Vance KW, Abrahams A, and Goding CR (2004). Tbx2 Directly Represses the Expression of the p21WAF1 Cyclin-Dependent Kinase Inhibitor. Cancer Res 64, 1669–1674. 10.1158/0008-5472.Can-03-3286. [PubMed: 14996726]
- 31. Walston H, Iness AN, and Litovchick L (2021). DREAM On: Cell Cycle Control in Development and Disease. Annu. Rev. Genet 55, 309–329. 10.1146/annurev-genet-071819-103836. [PubMed: 34496610]
- 32. Chen X, Müller GA, Quaas M, Fischer M, Han N, Stutchbury B, Sharrocks AD, and Engeland K (2013). The Forkhead Transcription Factor FOXM1 Controls Cell Cycle-Dependent Gene Expression through an Atypical Chromatin Binding Mechanism. Mol. Cell Biol 33, 227–236. 10.1128/MCB.00881-12. [PubMed: 23109430]
- 33. Chen H, Li C, Peng X, Zhou Z, Weinstein JN, and Cancer Genome Atlas Research Network; and Liang, H. (2018). A Pan-Cancer Analysis of Enhancer Expression in Nearly 9000 Patient Samples. Cell 173, 386–399.e12. 10.1016/j.cell.2018.03.027. [PubMed: 29625054]
- 34. Zhang Z, Lee JH, Ruan H, Ye Y, Krakowiak J, Hu Q, Xiang Y, Gong J, Zhou B, Wang L, et al. (2019). Transcriptional landscape and clinical utility of enhancer RNAs for eRNA-targeted therapy in cancer. Nat. Commun 10, 4562. 10.1038/s41467-019-12543-5. [PubMed: 31594934]
- 35. Tan SH, Leong WZ, Ngoc PCT, Tan TK, Bertulfo FC, Lim MC, An O, Li Z, Yeoh AEJ, Fullwood MJ, et al. (2019). The enhancer RNA ARIEL activates the oncogenic transcriptional program in

- T-cell acute lymphoblastic leukemia. Blood 134, 239–251. 10.1182/blood.2018874503. [PubMed: 31076442]
- 36. Liang J, Zhou H, Gerdt C, Tan M, Colson T, Kaye KM, Kieff E, and Zhao B (2016). Epstein-Barr virus super-enhancer eRNAs are essential for MYC oncogene expression and lymphoblast proliferation. Proc. Natl. Acad. Sci. USA 113, 14121–14126. 10.1073/pnas.1616697113. [PubMed: 27864512]
- 37. Schneider CA, Rasband WS, and Eliceiri KW (2012). NIH Image to ImageJ: 25 years of image analysis. Nat. Methods 9, 671–675. [PubMed: 22930834]
- 38. Khaitan D, Dinger ME, Mazar J, Crawford J, Smith MA, Mattick JS, and Perera RJ (2011). The melanoma-upregulated long noncoding RNA SPRY4-IT1 modulates apoptosis and invasion. Cancer Res 71, 3852–3862. 10.1158/0008-5472.Can-10-4460. [PubMed: 21558391]
- 39. Batish M, and Tyagi S (2019). Fluorescence In Situ Imaging of Dendritic RNAs at Single-Molecule Resolution. Curr. Protoc. Neurosci 89, e79. 10.1002/cpns.79. [PubMed: 31532916]
- 40. Koppula A, Abdelgawad A, Guarnerio J, Batish M, and Parashar V (2022). CircFISH: A Novel Method for the Simultaneous Imaging of Linear and Circular RNAs. Cancers 14, 428. 10.3390/cancers14020428. [PubMed: 35053590]
- 41. Lai LT, Lee PJ, and Zhang LF (2013). Immunofluorescence protects RNA signals in simultaneous RNA-DNA FISH. Exp. Cell Res 319, 46–55. 10.1016/j.yexcr.2012.11.009. [PubMed: 23164508]
- 42. Takei Y, Yun J, Zheng S, Ollikainen N, Pierson N, White J, Shah S, Thomassie J, Suo S, Eng CHL, et al. (2021). Integrated spatial genomics reveals global architecture of single nuclei. Nature 590, 344–350. 10.1038/s41586-020-03126-2. [PubMed: 33505024]
- 43. Neal CJ, Sakthivel TS, Fu Y, and Seal S (2021). Aging of Nanoscale Cerium Oxide in a Peroxide Environment: Its Influence on the Redox, Surface, and Dispersion Character. J. Phys. Chem C 125, 27323–27334. 10.1021/acs.jpcc.1c06279.
- 44. El Ghzaoui C, Neal CJ, Kolanthai E, Fu Y, Kumar U, Hu J, Zgheib C, Liechty KW, and Seal S (2022). Assessing the bio-stability of micro-RNA-146a conjugated nanoparticles via electroanalysis. Nanoscale Adv 5, 191–207. 10.1039/d2na00600f. [PubMed: 36605803]
- 45. Fu Y, Kolanthai E, Neal CJ, Kumar U, Zgheib C, Liechty KW, and Seal S (2022). Engineered Faceted Cerium Oxide Nanoparticles for Therapeutic miRNA Delivery. Nanomaterials 12, 4389. 10.3390/nano12244389. [PubMed: 36558243]

Highlights

- *Inc-HLX-2-7* functions as an enhancer RNA to control HLX expression
- A positive feedback loop between *Inc-HLX-2-7*, HLX, and MYC promotes group 3 medulloblastoma
- ASOs targeting *lnc-HLX-2-7* repress tumor growth, especially in combination with cisplatin

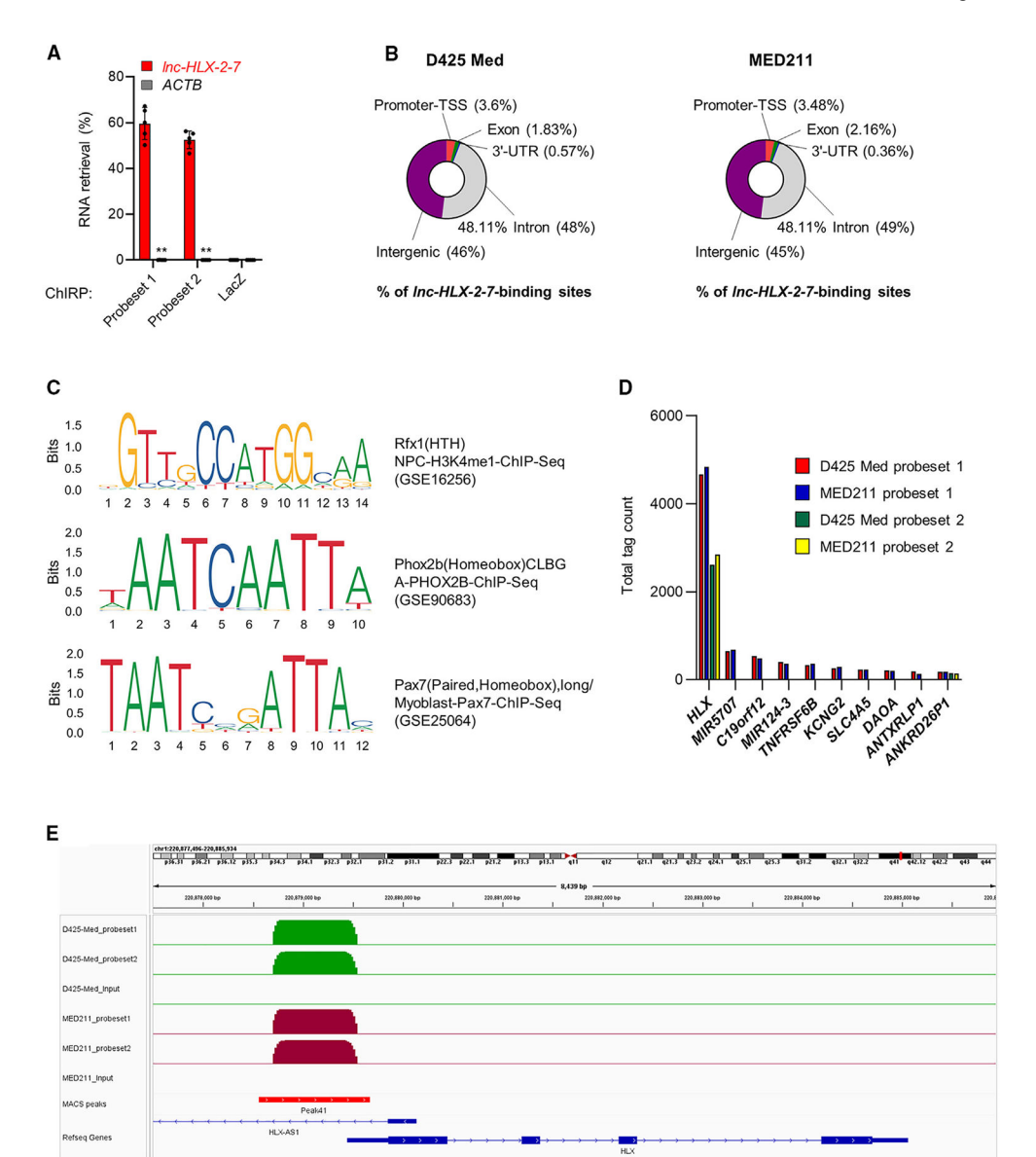


Figure 1. *Inc-HLX-2-7* RNA specifically accumulates in the HLX promoter region (A) Biotinylated *Inc-HLX-2-7* antisense DNA probes retrieved approximately 60% of total

- *Inc-HLX-2-7* RNA. Biotinylated *LacZ* antisense DNA probes did not retrieve RNA. n = 5, **p < 0.01 by two-tailed Student's t test. Data are expressed as mean \pm SE. The probe set for the odd group is probe set 1, and the probe set for the even group is probe set 2. *ACTB* was used as a negative control RNA.
- (B) Percentage of *Inc-HLX-2-7*-binding sites localized to different regions within the genome.
- (C) Summary of the top-scoring motifs among *Inc-HLX-2-7*-binding sites.
- (D) Total tag count of *Inc-HLX-2-7* ChIRP-seq.
- (E) ChIRP-seq tag density at the *HLX* gene promoter. Data are represented as *Inc-HLX-2-7*-pull-down compared with input controls. Track heights were normalized to allow for comparison between groups. *Inc-HLX-2-7* pull-down data were generated from overlapping

peak data from biological replicates of *Inc-HLX-2-7*-probeset1 pull-down and *Inc-HLX-2-7*-probeset2 pull-down samples compared with input. Aligned reads were used for peak calling of the ChIRP regions using MACS v.1.4.0. Statistically significant ChIRP-enriched regions (peaks) were identified by comparison with input, using a p value threshold of 10^{-5} . ChIRP, chromatin isolation by RNA purification; TSS, transcription start site; UTR, untranslated region.

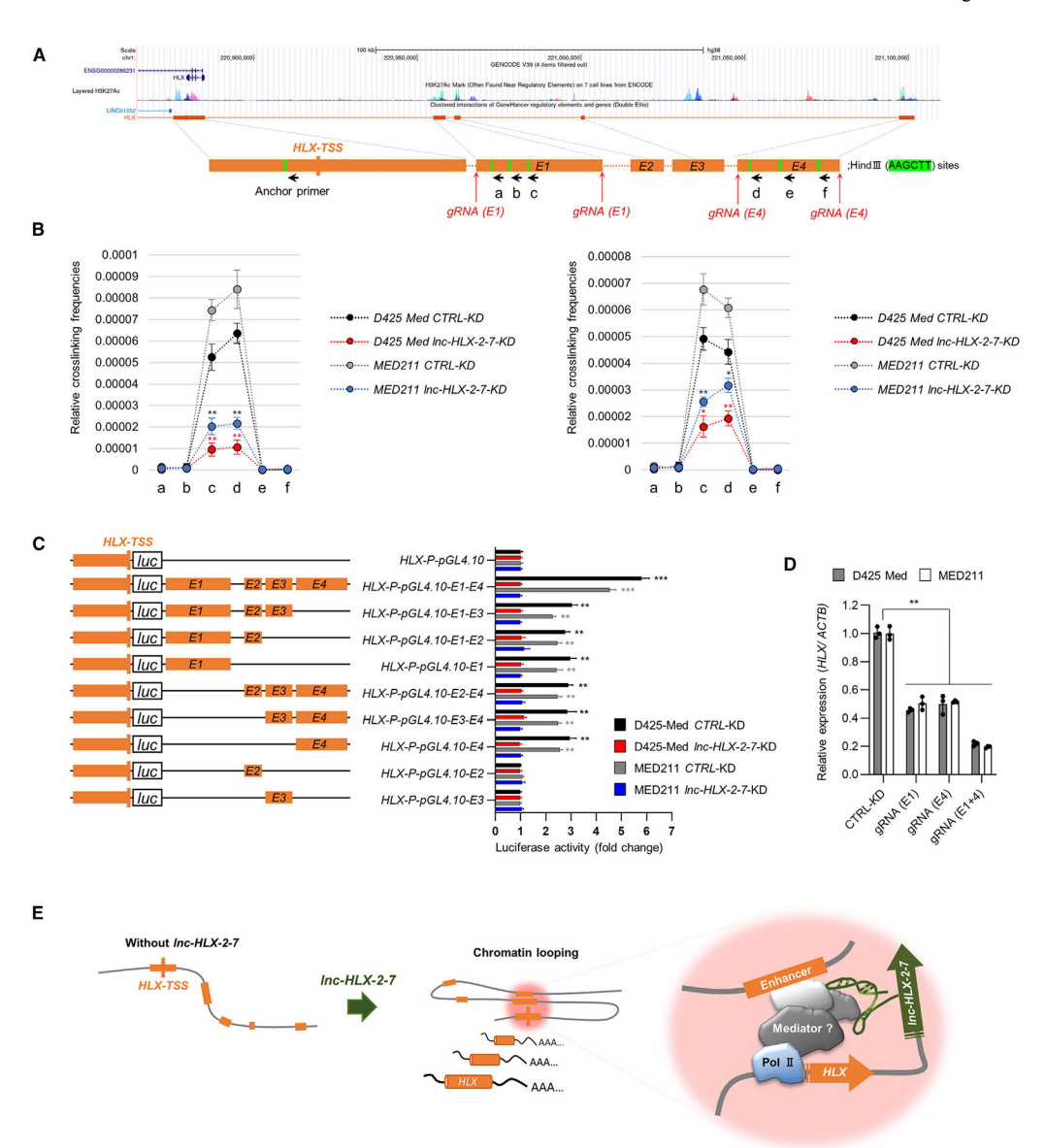


Figure 2. *Inc-HLX-2-7* activates HLX expression by recruiting surrounding enhancer elements (A) Schematic of the genomic context of the *HLX* promoter and surrounding enhancer elements (E1, E2, E3, and E4) according to the UCSC Genome Browser and GeneHancer.²⁰ The *HLX*-enhancer region predicted by GeneHancer is indicated by an orange bar. Positions of HindIII restriction target fragments are marked by green bars, and 3C primers (a, b, c, d, e, f, and anchor primers) were designed accordingly. Red arrows indicate the position of the single guide RNAs (sgRNAs) designed to target the E1 and E4 elements.

- (B) 3C assay showing association between the *HLX* promoter and surrounding enhancer elements (E1, E2, E3, and E4) in control and *Inc-HLX-2-7*-KD MB cells.
- (C) Schematic of HLX promoter-luciferase constructs. Right, luciferase reporter activity in control and Inc-HLX-2-7-KD MB cells. Inclusion of the E1 and E4 elements led to robust enhancement of promoter activity, which was significantly attenuated in Inc-HLX-2-7-KD cells. n = 3, **p < 0.01 and ***p < 0.001 by two-tailed Student's t test.

(D) qPCR analysis of *HLX* mRNA in control MB cells and three independent E1- and E4-targeted clones. Expression values were normalized to *ACTB* internal controls. Cell culture experiments were repeated at least three times. n = 3, **p < 0.01, Kruskal-Wallis analysis. Data are expressed as mean \pm SE.

(E) A model of *Inc-HLX-2-7*-mediated chromatin looping on transcriptional activation of *HLX*. 3C, chromatin conformation capture; ACTB, β -actin; CTRL, control; KD, knockdown; luc, luciferase; MB, medulloblastoma; qPCR, quantitative polymerase chain reaction.

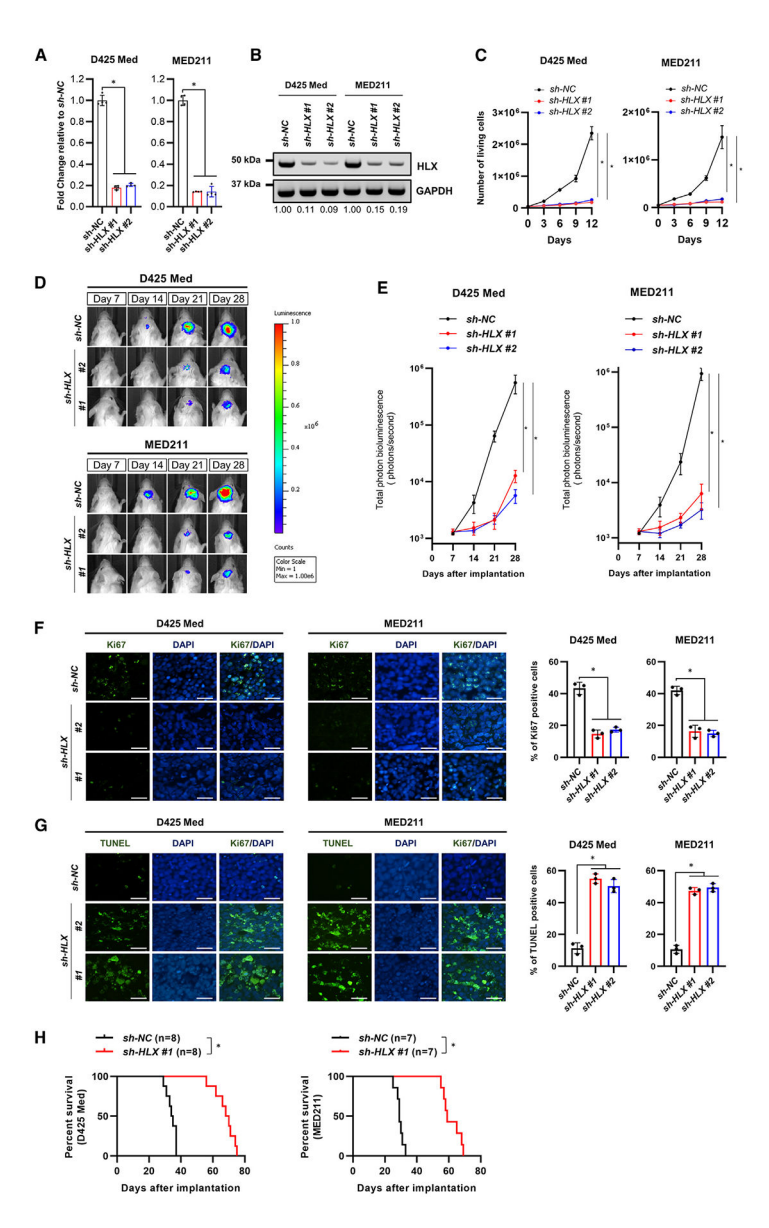


Figure 3. HLX promotes tumorigenicity of G3 MB

- (A) mRNA expression of HLX in D425 Med and MED211 cells with negative control shRNA (sh-NC) or sh-HLX for HLXKD. Relative expression level to sh-NC is indicated on the y axis. n = 4, *p < 0.01, Kruskal-Wallis analysis.
- (B) Protein expression of HLX in D425 Med and MED211 cells with sh-NC or sh-HLX. Quantified band densities are presented below the images as relative values (HLX/GAPDH).
- (C) Cell viability assays were performed with D425 Med and MED211 sh-NC (control) and sh-HLX cells. Points represent the mean and standard deviation of three biological replicates. n = 4, *p < 0.01, Kruskal-Wallis analysis.
- (D and E) Luciferase-expressing D425 Med and MED211 cells with sh-NC (control) and sh-HLX were implanted into the cerebellums of NOD-SCID mice; tumor formation was assessed by bioluminescence imaging. Changes in bioluminescent signal were examined weekly after tumor implantation. (E) Quantification of total photon counts from mice

implanted with D425 Med and MED211 containing sh-NC or sh-HLX. n = 5, *p < 0.01, Kruskal-Wallis analysis.

(F and G) Ki67 (F) and TUNEL (G) staining of xenograft tumors. Nuclei are stained with DAPI. Scale bars, 50 μ m. Quantification of Ki67- and TUNEL-positive cells is shown on the right. *p < 0.01, Kruskal-Wallis analysis.

(H) Overall survival was determined by Kaplan-Meier analysis; the log-rank test was applied to assess the differences between groups. *p < 0.05 by Mantel-Cox log-rank test. GAPDH, glyceraldehyde 3-phosphate dehydrogenase; MB, medulloblastoma; NC, negative control.

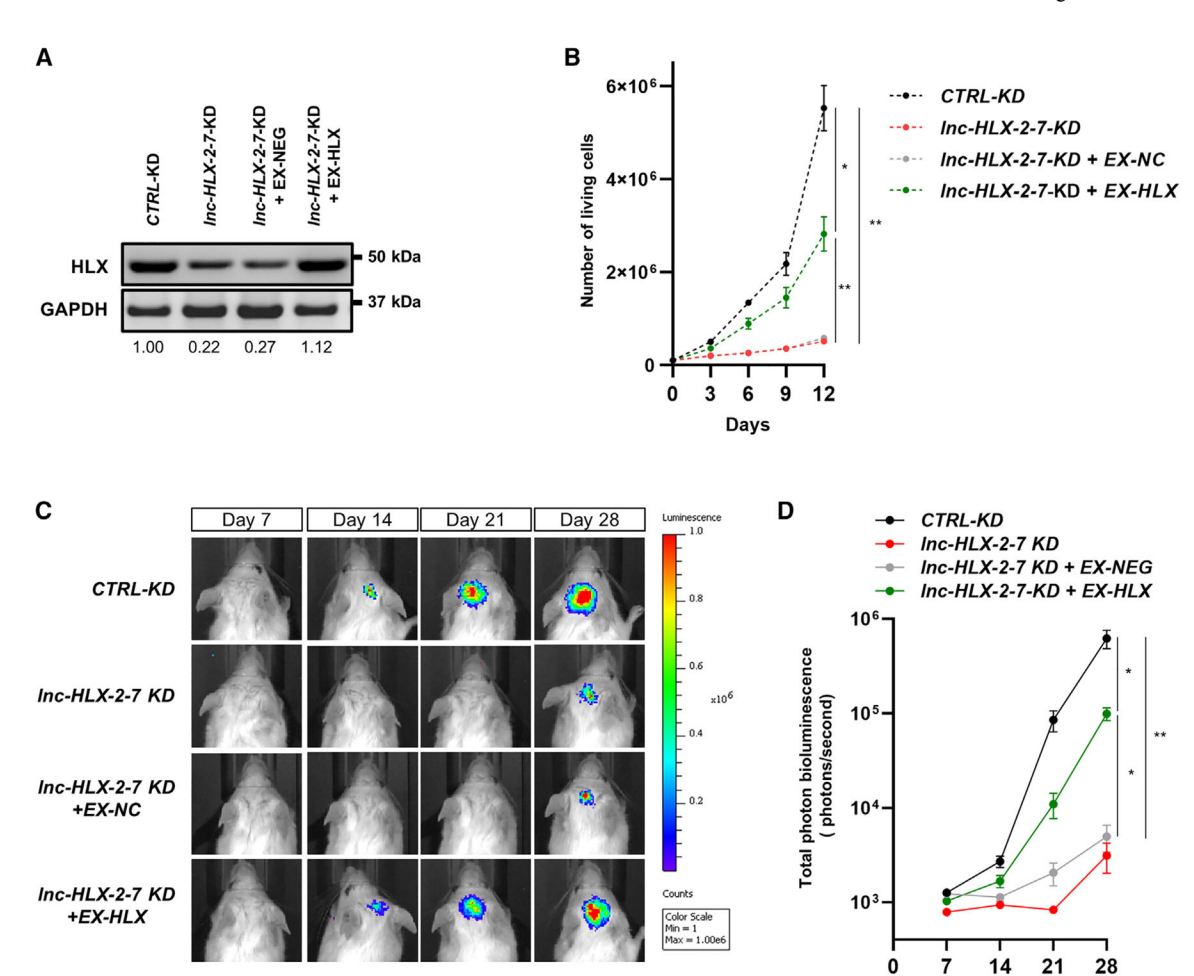


Figure 4. HLX rescues G3 MB cell phenotypic changes caused by *Inc-HLX-2-7* inhibition (A) Western blot analysis for HLX expression in D425 Med cells containing CTRL-KD, *Inc-HLX-2-7*-KD, *Inc-HLX-2-7*-KD + EX-NC, and *Inc-HLX-2-7*-KD + EX-HLX. Quantified band densities are presented below the images as relative values (HLX/GAPDH). (B) Cell viability assays performed with D425 Med cells containing CTRL-KD, *Inc-HLX-2-7*-KD, *Inc-HLX-2-7*-KD + EX-NC, and *Inc-HLX-2-7*-KD + EX-HLX. Points represent the mean and standard deviation of three biological replicates. n = 4, *p < 0.01 by Kruskal-Wallis analysis.

Days after implantation

(C) Luciferase-expressing D425 Med cells containing CTRL-KD, *Inc-HLX-2-7*-KD, *Inc-HLX-2-7*-KD + EX-NC, and *Inc-HLX-2-7*-KD + EX-HLX were implanted into the cerebellums of NOD-SCID mice; tumor formation was assessed by bioluminescence imaging. Changes in bioluminescent signal were examined weekly after tumor implantation. (D) Quantification of total photon counts from mice implanted with D425 Med cells containing CTRL-KD, *Inc-HLX-2-7*-KD, *Inc-HLX-2-7*-KD + EX-NC, and *Inc-HLX-2-7*-KD + EX-HLX. n = 5; results are presented as the mean ± SEM. *p < 0.05 by one-way ANOVA with Bonferroni post hoc tests. CTRL, control; EX, expressing; GAPDH, glyceraldehyde 3-phosphate dehydrogenase; KD, knockdown; MB, medulloblastoma; NC, negative control.

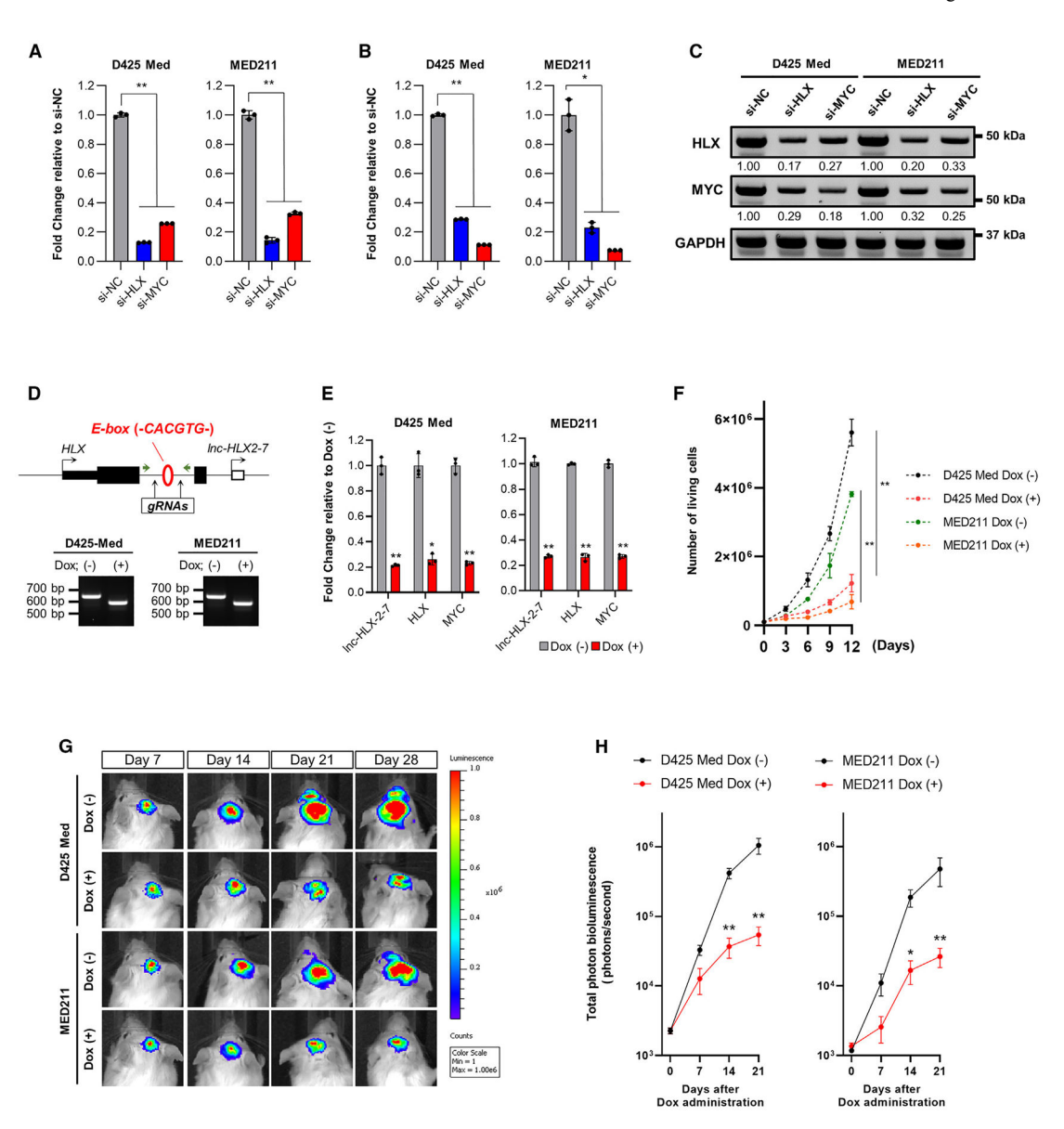


Figure 5. A *Inc-HLX-2-7*, HLX, and MYC positive feedback loop strongly promotes G3 MB (A and B) mRNA expression of HLX (A) and MYC (B) in D425 Med and MED211 cells treated with small interfering RNAs (siRNAs) targeting the genes indicated in the x axis. Relative expression level to siRNA-NC (si-NC) is indicated on the y axis. n = 3, *p < 0.01 by Kruskal-Wallis analysis.

- (C) Protein expression of HLX and MYC in D425 Med and MED211 cells treated with si-NC, si-HLX, or si-MYC. Quantified band densities are presented below the images as relative values (HLX/GAPDH and MYC/GAPDH).
- (D) Schematic showing E-box motifs around the transcription start site of *Inc-HLX-2-7*. Open circles indicate E-box motifs. Black arrows indicate the position of the sgRNAs designed to target the E-box. Green arrows show the location of primers used for PCR to determine E-box deletion. Agarose gel electrophoresis revealed E-box loss in D425 Med and MED211 cell lines after addition of doxycycline (Dox).

(E) Expression of *MYC*, *HLX*, and *Inc-HLX-2-7* in D425 Med and MED211 cells with (Dox (+)) and without Dox (Dox (-)). Values are indicated relative to abundance in Dox (-) cells. *p < 0.01 by Kruskal-Wallis analysis.

- (F) Cell viability assays performed with D425 Med and MED211 cells with and without Dox. Points represent the mean and standard deviation of three biological replicates. *p < 0.01 by Kruskal-Wallis analysis.
- (G) Dox-dependent E-box-deletion D425 Med and MED211 cells expressing luciferase were implanted into the cerebellums of NOD-SCID mice, and tumor formation was assessed by bioluminescence imaging. Changes in bioluminescent signal were examined weekly after the addition of Dox.
- (H) Quantification of total photon counts from mice implanted with D425 Med and MED211 cells with and without Dox. n = 5; results are presented as the mean \pm SEM. *p < 0.05 by one-way ANOVA with Bonferroni post hoc tests. GAPDH, glyceraldehyde 3-phosphate dehydrogenase; MB, medulloblastoma.

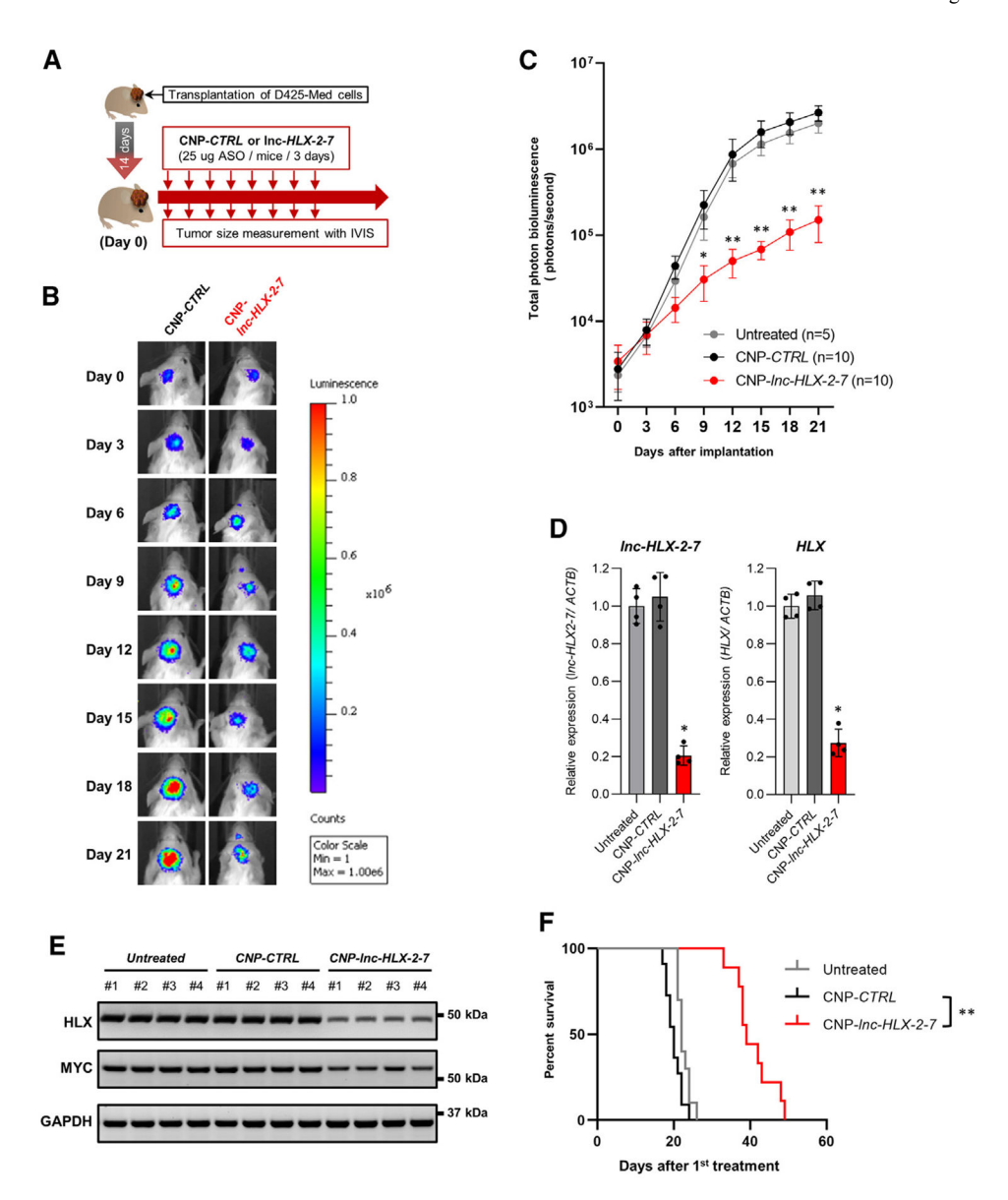


Figure 6. CNP-Inc-HLX-2-7 efficiently represses tumor growth in an intracranial MB xenograft mouse model

- (A) Schematic showing the treatment paradigm in the MB xenograft mouse model. D425 Med cells were injected into the brains of NOD-SCID mice. After 14 days, mice were treated with CNP-CTRL or CNP-*Inc-HLX-2-7* every 3 days for 24 days.
- (B) Tumor formation was assessed by bioluminescence imaging every 3 days after treatment.
- (C) Quantification of total photon counts from mice treated with CNP-CTRL or CNP-*Inc-HLX-2-7*. n=10; results are presented as the mean \pm SEM. *p < 0.05 and **p < 0.01 by one-way ANOVA with Bonferroni post hoc test.
- (D and E) Quantitative PCR analysis for Inc-HLX-2-7 and HLX (D) and western blot analysis for HLX and MYC (E) expression in mouse xenografts; results are presented as mean \pm SEM. n = 4, *p < 0.05 by one-way ANOVA with Bonferroni post hoc test.

(F) Overall survival was determined by Kaplan-Meier analysis, and the log-rank test was applied to assess the differences between groups. *p < 0.05 by Mantel-Cox log-rank test. CNP, cerium oxide nanoparticle; CTRL, control; IVIS, *in vivo* spectral imaging system; MB, medulloblastoma.

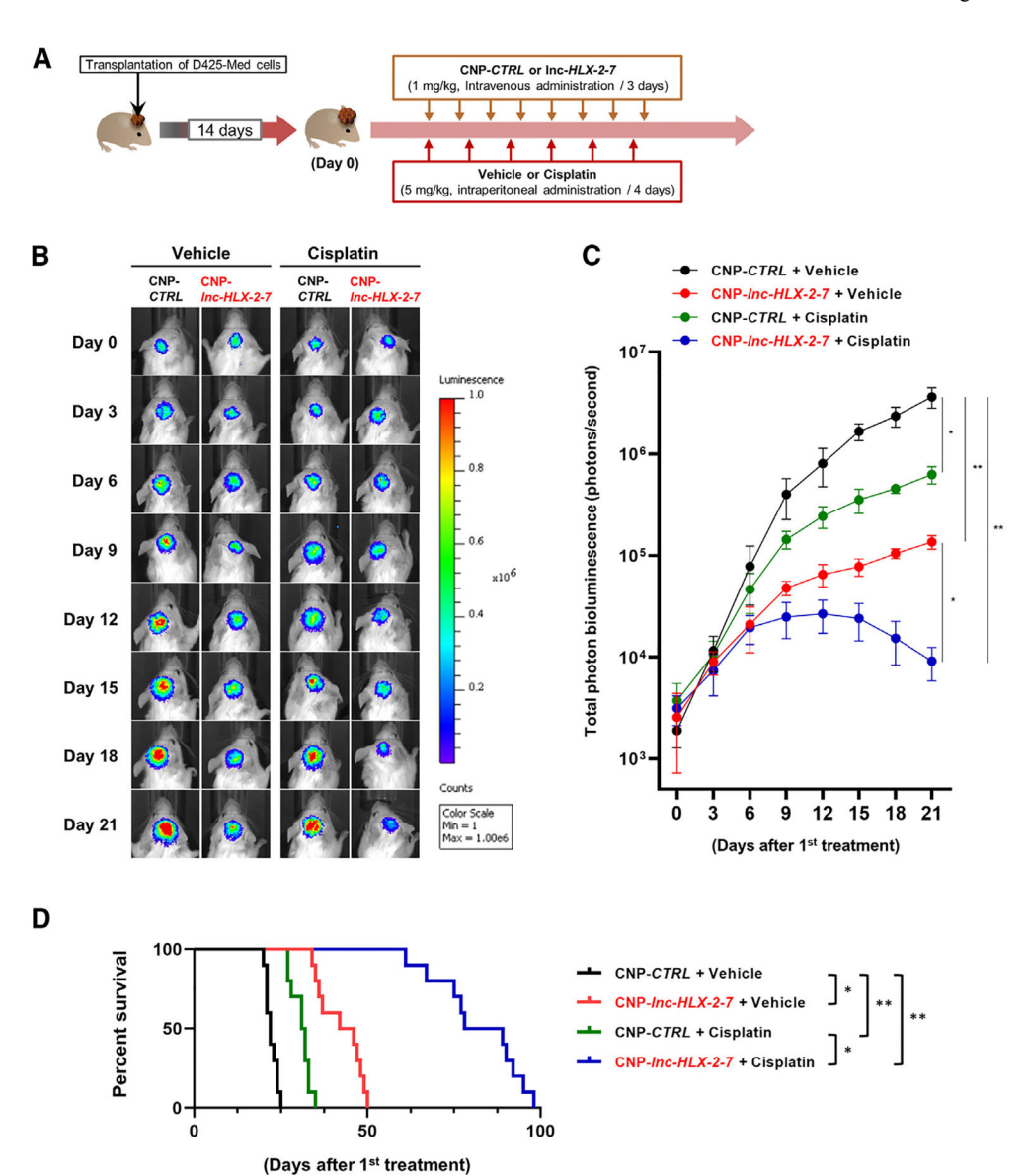


Figure 7. Combination therapy with CNP-lnc-HLX-2-7 and cisplatin inhibits tumor growth and prolongs mouse survival

- (A) Schematic showing the treatment paradigm in the MB xenograft mouse model. D425 Med cells were implanted into the brains of NOD-SCID mice. After 14 days, mice were treated with CNP-CTRL + DMSO, CNP-*Inc-HLX-2-7*+ DMSO, CNP-CTRL + cisplatin, or CNP-*Inc-HLX-2-7*+ cisplatin every 3 days (CNP-CTRL or CNP-*Inc-HLX-2-7*) or 4 days (DMSO or cisplatin) for 24 days.
- (B) Tumor formation was assessed by bioluminescence imaging every 3 days after treatments.
- (C) Quantification of total photon counts from mice treated with CNP-CTRL + DMSO, CNP-Inc-HLX-2-7+ DMSO, CNP-CTRL + cisplatin, or CNP-Inc-HLX-2-7+ cisplatin. n = 10; results are presented as the mean \pm SEM. *p < 0.05 and **p < 0.01 by two-way ANOVA with Bonferroni post hoc test.

(D) Overall survival was determined by Kaplan-Meier analysis, and the log-rank test was applied to assess the differences between groups. *p < 0.05 and **p < 0.01 by Mantel-Cox log-rank test. CNP, cerium oxide nanoparticle; CTRL, control; DMSO, dimethyl sulfoxide; MB, medulloblastoma.

KEY RESOURCES TABLE

Katsushima et al.

REAGENT or RESOURCE	SOURCE	IDENTIFIER
Antibodies		
Anti-HLX antibody	Sigma-Aldrich	Cat# HPA005968; RRID:AB_1079066
Anti-MYC antibody	Cell Signaling Technology	Cat# 5605; RRID:AB_1903938
Anti-cleaved Caspase-7 (Asp198) antibody	Cell Signaling Technology	Cat# 8438; RRID:AB_11178377
Anti-cleaved Caspase-3 (Asp175) antibody	Cell Signaling Technology	Cat# 9661; RRID:AB_437838
Anti-GAPDH antibody	Genetex	Cat# GTX100118; RRID:AB_1080976
Anti-Ki67 antibody (Alexa Fluor 488 conjugate)	Cell Signaling Technology	Cat# 11882; RRID:AB_2687824
Anti-NF90 antibody	Proteintech	Cat# 19887-1-AP; RRID:AB_10666431
Normal Rabbit IgG	MBL International	Cat# PM035; RRID:AB_10805234
anti-Cy5 antibody	Santa Cruz Biotechnology	Cat# sc-166896; RRID:AB_10607798
Chemicals, peptides, and recombinant pro	teins	
DMEM/F12	Thermo Fisher Scientific	Cat# 11320033
DMEM	Thermo Fisher Scientific	Cat# 12491015
Penicillin-streptomycin solution (100X)	Thermo Fisher Scientific	Cat# 15140122
B27 supplement	Thermo Fisher Scientific	Cat# 17504044
Fetal bovine serum	Thermo Fisher Scientific	Cat# 16140071
Heparin	Fisher Scientific	Cat# NC1357415
EGF	R&D Systems	Cat# 236-EG
bFGF	R&D Systems	Cat# 3718-FB-010
Streptavidin magnetic C1 beads	Thermo Fisher Scientific	Cat# 65001
Proteinase K	Sigma-Aldrich	Cat# 39450-01-6
RNase A	Thermo Fisher Scientific	Cat# 12091021
RNase H	Thermo Fisher Scientific	Cat# 18021071
HindIII	NEB	Cat# R0104
T4 DNA ligase	NEB	Cat# M0202
Lipofectamine 3000	Thermo Fisher Scientific	Cat# L3000001
Lipofectamine RNAiMAX	Thermo Fisher Scientific	Cat# 13778075
Blasticidin	InvivoGen	Cat# ant-bl-05
Puromycin	InvivoGen	Cat# ant-pr-1
Dynabeads Protein G	Thermo Fisher Scientific	Cat# 100-03D
RNase T1	Thermo Fisher Scientific	Cat# EN0541
Critical commercial assays		
ChIP DNA Clean and concentrator kit	Zymo Research	Cat# 11-379C
Direct-zol RNA Miniprep kit	Zymo Research	Cat# R2051
In-Fusion HD cloning kit	Takara Bio	Cat# 638947
Dual-Glo Luciferase Assay	Promega	Cat# E2920
Lenti-X [™] Packaging Single Shots	Takara Bio	Cat# 631278
ECL system	Thermo Fisher Scientific	Cat# 34579

Page 31

Katsushima et al.

DeadEnd™ Fluorometric TUNEL	SOURCE	IDENTIFIER
System	Promega	Cat# G3250
RiboTrap kit	MBL International	Cat# RN1011
MEGAstrip T7 system	Thermo Fisher Scientific	Cat# AM1334
RiboCluster Profiler RIP-Assay kit	MBL International	Cat# RN1005
Deposited data		
RNA-seq data	NCBI GEO	GSE188746
ChIRP-seq data	NCBI GEO	GSE232749
Experimental models: Cell lines		
D425 Med	Dr. Charles G. Eberhart lab	RRID:CVCL_1275
MED211	Dr. Charles G. Eberhart lab	N/A
DAOY	ATCC	Cat# HTB-186
CHLA01 Med	ATCC	Cat# CRL-3021
Experimental models: Organisms/strains		
NOD-SCID mice	Jackson Laboratory	Strain # 001303
Oligonucleotides		
qPCR primers (see Table S2)	This study	N/A
DNA-RNA-FISH probe sets (see Table S3)	This study	N/A
ASO targeting lnc-HLX-2-7 (ASO- <i>lnc-HLX-2-7</i>)	This study	5' to 3' +T*+G*+A*G*A*G*A*T*T*A* A*T*C*T*A*G*A*T*+T*+G*+C The PS linkages are indicated with asterisks (*), and LNA- modified oligonucleotides are indicated with plus signs (+).
Control ASO (ASO-CTRL)	This study	5' to 3' +T*+C*+G*A*A*G*T*A*C*T* C*A*G*C*G*T*A*A*+G*+T*+T The PS linkages are indicated with asterisks (*), and LNA- modified oligonucleotides are indicated with plus signs (+).
siRNA targeting HLX	Thermo Fisher Scientific	Assay ID: s6639
siRNA targeting MYC	Thermo Fisher Scientific	Assay ID: s9129
Silencer [™] Select Negative Control No. 1 siRNA	Thermo Fisher Scientific	Cat# 4390843
Recombinant DNA		
HLX-knockdown lentivirus plasmids	GeneCopoeia	Cat# HSH100211-LVRU6GP
shRNA Scrambled Control lentivirus plasmids	GeneCopoeia	Cat# CSHCTR001-LVRU6GP
HLX-expressing lentivirus plasmids	GeneCopoeia	Cat# EX-OL00749-LX304
Negative control lentivirus plasmids	GeneCopoeia	Cat# EX-NEG-LX304
pGL4.10 vector	Promega	Literature # 9PIE665
Software and algorithms		
ImageJ	Schneider et al. ³⁷	https://imagej.nih.gov/ij/
	http://www.graphpad.com/	RRID: SCR_002798
GraphPad Prism v9		
GraphPad Prism v9 Stellaris smFISH probe designer	http://biosearch.com/	N/A
*	http://biosearch.com/ National Library of Medicine	N/A https://blast.ncbi.nlm.nih.gov/Blast.cgi

Page 32

Katsushima et al.

microscope

REAGENT or RESOURCE SOURCE IDENTIFIER Molecular Devices Metamorph imaging software https://www.moleculardevices.com/products/cellular-imagingsystems/acquisition-and-analysis-software/metamorph-microscopy https://digitalinsights.qiagen.com/products-overview/discovery-insights-portfolio/analysis-and-visualization/qiagen-ipa/Ingenuity Pathway Analysis Qiagen Other IVIS Lumina II N/A Xenogen Bioruptor 300 N/A Diagenode GloMax 20/20 luminometer Promega N/A N/A Nikon C1 confocal system Nikon Covaris S220 system Covaris N/A CX-2000 Ultraviolet Crosslinker UVP N/A Nikon TiE inverted fluorescence Nikon N/A

Page 33